The Detection of Series Arc Fault in Photovoltaic Systems Based on the Arc Current Entropy

Nikola L. Georgijevic, Marko V. Jankovic, *Senior Member, IEEE*, Srdjan Srdic, *Member, IEEE*, and Zoran Radakovic

***Abstract*—This paper presents a series arc-fault detection algorithm for photovoltaic (PV) systems, which relies on the quantum probability model theory. The algorithm determines the presence of the arc by calculating the modified Tsallis entropy of the PV panel current. Based on the calculated entropy, the algorithm is able to differentiate an arc state (when the current variations are chaotic) from a no-arc state (when the current variations are ordered). The proposed algorithm enables arc-fault detection on a plug-and-play principle, requiring no prior information about the PV system in which it operates. The operation of the algorithm was first simulated on the prerecorded data from the system with the PV panel simulator and the commercial PV inverter. A laboratory prototype of the detector was then built and tested in a real 1.6-kW grid-connected PV system with different PV inverter, without any additional parameter adjustments. Both the sensitivity and the robustness of the detector were confirmed. The tests have shown that both the sustained series arcs and the small sparking series arcs were successfully detected, and there was no false detection due to the MPP tracker operation, PV current step change, or inverter turn on transient.**

***Index Terms*—Arc discharges, entropy, fault diagnosis, photovoltaic (PV) power systems.**

I. Introduction

ELECTRICAL power generation from photovoltaic (PV) systems has been growing continuously over the last 30 years. Starting from small-scale niche applications in the early 80's, PV systems have become one of the mainstream renewable power sources. Just in the last ten years, more than 174 GW of PV systems were installed globally, and around 40 GW were installed in 2014 alone [1]. Since modern PV systems can have complex structures with large number of electrical contacts and with dc voltages reaching 1000 V, there is a considerable risk of hazardous situations initiated by the occurrence of an electric arc. In [2], electric arcs in PV systems are classified in three groups: series, parallel, and ground arcs. Series arcs can appear at a breakpoint of a conductor or at a bad connection point in a circuit. Parallel arcs may occur between conductors with different potentials, and ground arcs may occur in situations where a current path is formed through ground. Methods for differentiating series and parallel PV arcs are presented in [3]. Being a high-temperature plasma, electric arc can significantly damage and/or ignite electric insulation and other surrounding objects [4]. In order to prevent hazards caused by electric arc, National Electrical Code (NEC) requires that every PV system in the U.S. operating with maximum dc voltage higher than 80 V must be protected from arc faults [5]. According to [6], working group 2 of IEC committee works on a publication regarding arc-fault detection devices (AFDD) in dc circuits.

In all electrical circuits which are compliant with the NEC 2011, the overcurrent protection devices are set to current which is 56% higher than the maximum nominal current at protection device location [7]. Since a dc current of a series electric arc (SEA) cannot be higher than the maximum dc current under normal (unfaulted) operating conditions (SEA cannot backfeed current into a fault), standard overcurrent protection devices cannot be used to detect an SEA [2], [7]. Similar problem is observed in cases where a parallel electric arc current is lower than the nominal current [8].

Many arc-fault detection methods for PV systems have been presented in the literature. A comparative summary of different PV-fault detection techniques is presented in [9]. The detection algorithm, which is based on monitoring of the dc voltage at the inverter input terminals, and the corresponding autonomous series and parallel arc-fault detector are presented in [10]. The detector consists of two coupled resonant circuits, tuned to a frequency of a few 100 kHz. In case when an arc is present, a high-frequency voltage component is detected in those circuits, and the arc presence is signaled after certain checks. However, the standalone version of the detector had falsely detected an arc in some cases during inverter startup and turn-off procedures, and an intelligent detection unit was proposed in order to overcome those problems.

An intelligent protection device for integration into PV modules is presented in [11]. To detect an arc, the device uses a sudden increase in variance of the inverter input dc voltage when the arc is present. The detector is also able to short-circuit the PV panel terminals; thus, protecting the system from series and parallel arc faults, excluding the series arc faults inside the panel. The detector was able to detect an arc within 175 μs of its appearance in a simple circuit where the PV panel was modeled by the series connection of a variable dc source and a resistor. However, the detector was not tested in an actual PV power plant, and the inverter-generated noise was not taken into account.

An algorithm based on wavelets decomposition of PV panel current is presented in [12], where normalized RMS value

Manuscript received March 12, 2015; revised June 10, 2015 and August 18, 2015; accepted September 28, 2015. Date of publication October 12, 2015; date of current version March 2, 2016. Recommended for publication by Associate Editor F. H. Khan.

N. L. Georgijevic is with the School of Electrical Engineering and Electrical Engineering Institute Nikola Tesla, University of Belgrade, Belgrade 11000, Serbia (e-mail: nikola.georgijevic@ieent.org).

M. V. Jankovic is with the Electrical Engineering Institute Nikola Tesla, University of Belgrade, Belgrade 11000, Serbia (e-mail: elmarkoni@ieent.org).

S. Srdic and Z. Radakovic are with the School of Electrical Engineering, University of Belgrade, Belgrade 11100, Serbia (e-mail: srdic@etf.rs; radakovic@etf.rs).

Color versions of one or more of the figures in this paper are available online at http://ieeexplore.ieee.org.

Digital Object Identifier 10.1109/TPEL.2015.2489759

(calculated from the coefficients of wavelet decomposition) of a certain frequency subband and the dc current change are used for the arc-fault detection. Experimental results with simple test system were presented and it was shown that the algorithm is robust to the load step changes. However, the detector needed to be calibrated based on the prerecorded experimental data from the actual system for a predefined set of test conditions, and the influence of the PV inverter-generated noise on the detector operation was not evaluated. It is demonstrated in [13] that common types of faults in PV arrays (including line-to-line faults under low irradiance, line-to-line faults with high fault impedance, open-circuit faults, degradation faults, and moving partial shadings), which can lead to arcing and fire hazard, may not be cleared by traditional overcurrent protecting devices, like fuses. Three different outlier detection rules are presented with experimental results: 3-sigma, Hampel identifier, and Boxplot rule. It was concluded that the Boxplot rule performs best in identifying faults, while the 3-sigma method failed to detect any fault.

The detection of an electric arc fault in a PV system is often realized by registering changes in frequency spectrum of PV panel's current, which are caused by the electric arc [14]–[17]. The arcing noise is superimposed to the nonarcing noise, and the noise generated by the arc has pink noise characteristics (the power spectral density of the pink noise is inversely proportional to the frequency of the signal) [14], [15]. According to [15] and [16], a frequency band from 0.1 to 100 kHz provides more information for SEA detection than the rest of the current spectrum. Additionally, the arc-fault location and detector location do not appreciably affect the probability of the detection [15]. It is concluded in [18] that wind induced vibrations can cause current oscilations with magnitude that can exceed 1% of it's dc value. The highest frequency of wind-induced vibrations in experiments conducted in [18] was below 20 Hz. The major drawback of the algorithms that monitor frequency spectrum to detect SEA is that they need to be calibrated for every particular PV system. That is because the difference between the current spectrums with and without a SEA changes with the operating conditions. A comprehensive study presented in [15] shows that the spectrum of the PV string current when the SEA is present depends on number of different factors, such as inverter generated noise, influence of conductors' length, number of contacts and PV panels in the current path, antena effects, crosstalk, and other effects. It was also shown that the location of the arc fault and/or detector have a little effect on the frequency spectrum of the panel current. Also, as concluded in [19], the AFDDs should be tested in a system with the real PV panels and not with the PV panel simulator, since the two systems would have significantly different spectral signatures. Consequently, frequency-based algorithm that is calibrated for one inverter and one set of operating conditions might not work properly under different operating conditions.

This paper presents a series arc-fault detection algorithm for PV systems, which relies on the quantum probability model theory. The algorithm monitors the PV panel current entropy, where the entropy is calculated based on the quantum probability model and the Born rule. Based on the calculated entropy, the algorithm is able to differentiate an arc state (when the current variations are chaotic) from a no-arc state (when the current variations are ordered). Effectiveness of the proposed algorithm is evaluated by simulations on the prerecorded data from the system with the PV panel simulator and the commercial PV inverter, and by the experimental verification in a 1.6-kW grid-connected PV system.

Section II presents fundamentals of the quantum probability model and the Born rule. The new detection algorithm is presented in Section III, and its experimental evaluation is presented in Section IV.

II. Fundamentals of the Quantum Probability Model and the Born Rule

A. Introduction

In this section, a short recapitulation of the quantum probability model and the Born rule is given, similar to forms in [20] and [21]. The quantum probability model takes place in a Hilbert space H of finite or infinite dimension [22]. A state is represented by a positive semidefinite linear mapping (a matrix $\boldsymbol{\rho}$) from this space to itself, with a trace of 1, i.e., $\forall \boldsymbol{\Psi} \in \mathrm{H}$ $\boldsymbol{\Psi}^{\mathrm{T}} \boldsymbol{\rho} \boldsymbol{\Psi} \geq 0$, Tr $(\boldsymbol{\rho}) = 1$. Such $\boldsymbol{\rho}$ is self-adjoint and is called a density matrix.

Since $\boldsymbol{\rho}$ is self-adjoint, its eigenvectors $\boldsymbol{\Phi}_i$ are orthonormal, and since it is positive semidefinite, its eigenvalues p_i are real and nonnegative $p_i \geq 0$. The trace of a matrix is equal to the sum of its eigenvalues, therefore $\sum_i p_i = 1$.

The equation $\boldsymbol{\rho} = \Sigma_{\mathrm{i}}\, p_{\mathrm{i}} \boldsymbol{\Phi}_{\mathrm{i}} \boldsymbol{\Phi}_{\mathrm{i}}{}^{\mathrm{T}}$ is interpreted as "the system is in state Φ_{i} with probability p_{i}." The state $\boldsymbol{\rho}$ is called the pure state if $\exists i$ s.t. $p_{\mathrm{i}} = 1$. In this case, $\boldsymbol{\rho} = \boldsymbol{\Psi} \boldsymbol{\Psi}^{\mathrm{T}}$ for some normalized state vector $\boldsymbol{\Psi}$, and the system is said to be in state $\boldsymbol{\Psi}$. Therefore, the most general density operator is in the form $\boldsymbol{\rho} = \Sigma_{\mathrm{k}}\, p_{\mathrm{k}} \boldsymbol{\Psi}_{\mathrm{k}} \boldsymbol{\Psi}_{\mathrm{k}}{}^{\mathrm{T}}$, where the coefficients p_k are nonnegative and add up to one, and Ψ_{k} represent pure states. We can see that this decomposition is not unique.

A measurement M with an outcome $\boldsymbol{z}$ in some set $\boldsymbol{Z}$ is represented by a collection of positive definite matrices $\{\boldsymbol{m_z}\}_{z \in \boldsymbol{Z}}$ such that $\sum_{z \in \boldsymbol{Z}} m_z = 1$ (1 is being the identity matrix in H). Applying measurement M to state $\boldsymbol{\rho}$ produces the outcome $\boldsymbol{z}$ with probability

$$p_{\boldsymbol{z}}(\boldsymbol{\rho}) = \mathrm{trace}(\boldsymbol{\rho}\, \boldsymbol{m_z}). \tag{1}$$

This is the Born rule. Most quantum models deal with a more restrictive type of measurement called the von Neumann measurement, which involves a set of projection operators $\boldsymbol{m}_{\mathrm{a}} = \boldsymbol{a}\boldsymbol{a}^{\mathrm{T}}$, for which $\boldsymbol{a}^{\mathrm{T}}\boldsymbol{a}' = \delta_{\mathrm{aa}}{}'$. In a modern language, von Neumann's measurement is a conditional expectation onto a maximal Abelian subalgebra of the algebra of all bounded operators acting on the given Hilbert space. As before, $\sum_{\boldsymbol{a} \in \boldsymbol{M}} \boldsymbol{a}\boldsymbol{a}^T = 1$. For this type of measurement, the Born rule takes a simpler form: $p_{\mathrm{a}}(\boldsymbol{\rho}) = \boldsymbol{a}^{\mathrm{T}} \rho \boldsymbol{a}$. Assuming $\boldsymbol{\rho}$ is a pure state, this can be simplified further to

$$p_a(\boldsymbol{\rho}) = \left(\boldsymbol{a}^T \boldsymbol{\Psi}\right)^2. \tag{2}$$

Therefore, we can see that, if the state is $\boldsymbol{\rho}$, the probability of the outcome of the measurement will be $\boldsymbol{a}$, which is actually

defined by the cosine square of the angle between vectors $\boldsymbol{a}$ and $\boldsymbol{\Psi}$, or $p_{\mathrm{a}}(\boldsymbol{\rho}) = \cos^2(\boldsymbol{a},\boldsymbol{\Psi})$.

Now, without loss of generality, let us assume that we are dealing with a random variable $\boldsymbol{x}$ that takes realizations from a set of observed D-dimensional (D could be equal to 1, like it is in this paper) data vectors $\{\boldsymbol{x}_{\mathrm{k}}\}$, $k \in \{1, \ldots, K\}$, which are sampled from some distribution in time instants $t = kT$ where k is already defined and T represents the sampling period. Then, we can define $p(\boldsymbol{x} = \boldsymbol{x}_{\mathrm{k}} \mid t = kT)$ as

$$p\left(\boldsymbol{x}_k\right) \stackrel{\mathrm{def}}{=} \frac{\|\boldsymbol{x}_{\boldsymbol{k}}\|_2^2}{\sum_{i=1}^{K} \|\boldsymbol{x}_{\boldsymbol{i}}\|_2^2} \tag{3}$$

where K represents the overall number of samples that are going to be analyzed. It is interesting to note that the only thing that we can conclude about the $p(\boldsymbol{x}_{\mathrm{k}})$ is that it is proportional to $\|\boldsymbol{x}_{\boldsymbol{k}}\|_2^2$. The sum in the denominator represents the energy of samples that are going to be analyzed—we actually do not know the value of that sum in any, but the final moment. However, we know that it represents some constant. We can easily see that the adopted probability measure fulfills the two conditions that are required for the probability function $f(z)$ (in our case $p(z)$) to be considered as a modified generalized probability measure [23]:

For each $\boldsymbol{z}$, $0 \leq f(\boldsymbol{z}) \leq 1$

$$\sum\nolimits_i f(z_i) = 1.$$

B. Tsallis Entropy as a Kind of Measure of the Signal Behavior

It is possible to use different generalizations of the traditional notion of entropy as a measure of the signal behavior, but in this paper, we focus only on the Tsallis entropy. The Tsallis entropy is defined by the following equation [24]:

$$E_{TS} = \frac{1 - \sum_{k=1}^{K} p\left(x_k\right)^q}{q - 1} \tag{4}$$

where $q > 0$ and x_k represents samples of the signal of interest, and $p(x_k)$ is defined by (3). For the simpler interpretation of E_{TS} in the microcontroller, the measure M can be defined as a linear function of E_{TS} by the following equation:

$$M = \sum_{k=1}^{K} p\left(x_k\right)^q = 1 - (q-1)\, E_{TS}. \tag{5}$$

The measure M represents signal intrinsic characteristic (SIC)—here it is obtained by linear transformation from Tsallis' entropy. However, it also can be obtained by linear/nonlinear transformations from some other entropy measures, which is out of the scope of this paper. In [25], the Tsallis entropy of the recorded samples in the sliding window of the proper size was used as a measure of the "behavior" of the motor current. A similar approach has been successfully used in several applications in the different contexts [26], [27]. Fig. 1 depicts the 50-Hz sinusoidal waveform and the corresponding value for M (which is constant for the pure 50 Hz sinusoid), with sample rate of 10 kHz, and with K and q set to 100 and 4, respectively. Value of K is chosen such that vector of K samples spans over a whole number of half periods of the lowest frequency sinusoid (in this case, it contains one half period of 50-Hz sinusoid).

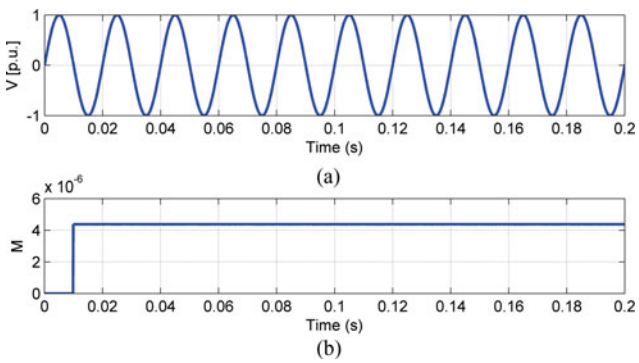

Fig. 1. (a) Pure sinusoidal signal and (b) the corresponding value M.

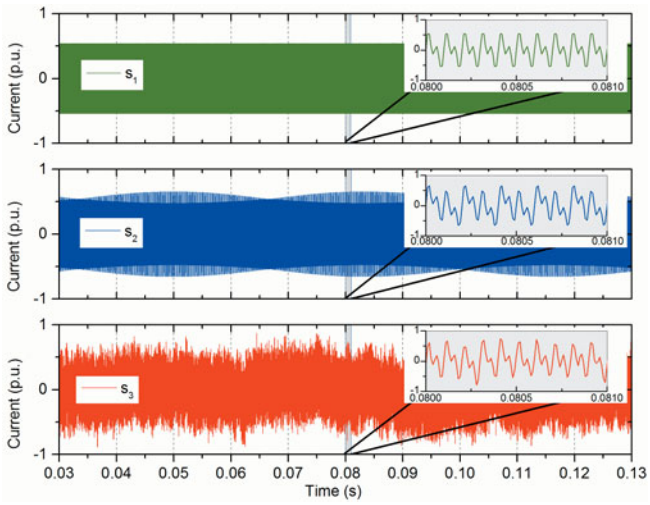

Fig. 2. Test signals for SIC evaluation: Signal s_1 (sum of 10- and 20-kHz sinusoids), signal s_2 (s_1 with added vibrations), and signal s_3 (s_1 with added pink noise).

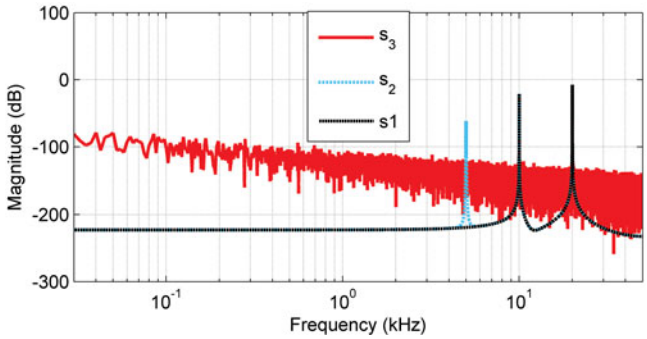

Fig. 3. Frequency spectrum of s_1, s_2, and s_3.

III. Proposed Detection Algorithm

A. Basic idea of the Proposed Algorithm

In order to illustrate how the proposed algorithm can differentiate between the normal operating conditions and the conditions with SEA, the SIC is evaluated for three synthetic signals that

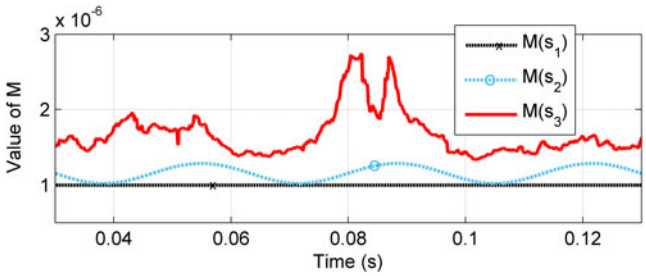

Fig. 4. M values calculated for signals s_1, s_2, and s_3.

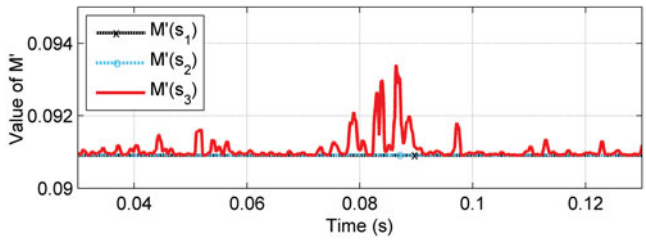

Fig. 5. M' values of signals s_1, s_2, and s_3, calculated from M values from Fig. 4.

represent (in a simplified manner) a PV panel current in a three different operating conditions. The first two signals (s_1 and s_2) are considered as representatives of normal operating conditions, and the third signal (s_3) represents the condition with a SAE. The dc component as well as all the frequency components below 100 Hz is not present in these signals, because those components are suppressed by the current measurement circuit in the algorithm implementation, as explained in more detail in Section IV. The first signal (s_1) is a sum of two higher frequency components—10 and 20 kHz sinusoid. These two components represent an inverter switching noise. The second signal (s_2) is made by adding a 5-kHz frequency component multiplied by 15-Hz sinusoid to the s_1. This signal represents noise signature changes that could be induced by some general 15-Hz vibrations. The third signal (s_3) is made by adding the pink noise (which represents an arc-generated noise) to the first signal (s_1), with a signal-to-noise ratio of 10 dB. The s_1 to s_2 ratio was also 10 dB. The waveforms and the frequency spectrums of s1, s2, and s3 are shown in Figs. 2 and 3.

The M values which are calculated for s_1, s_2, and s_3, after resampling all of them to 10 kHz, with $K = 100$ and $q = 4$, are shown in Fig. 4.

As can be seen from Fig. 4, the variance of the measure M for signal s_1 (signal with 10- and 20-kHz sinusoids) is small compared to the variance of M for signals s_2 and s_3. Moreover, M values of signal with vibration noise (s_2) change with dynamics of vibrations, and much slower than s_3 which changes stochastically. These results can be interpreted according to the common interpretation of entropy as a measure of disorder. Therefore, if a signal changes according to some pattern over some time interval (like s_1 does), it can be regarded as equally ordered over that time interval and its measure of disorder is constant. However, if signal pattern changes over some time interval, the entropy of that waveform will also change according to the change of pattern. On the other hand, if a pink-like noise is added to a signal, its measure of disorder increases and changes fast and stochastically as the noise changes. These features of M value are used to differentiate the regular operation (inverter switching with the disturbances caused by MPP tracker operation, moving clouds and wind induced vibrations) from the inverter operation with added pink (arc-fault-like) noise.

It is noted in [28] that same inverter models produce similar and reproducible switching noise under similar meteorological conditions, if same PV arrays are used. In other words, the inverter current changes according to some pattern. However, if meteorological conditions change, the operating conditions will also change as well as both the current noise signature and current behavior pattern [28]. If the current behavior pattern changes, the M value will change too (as s_2 in Fig. 4). These changes can be caused by moving clouds or by moving shadows (in a frequency range below 1 Hz), or by wind induced mechanical vibrations with frequencies up to 20 Hz [18]. In order to eliminate this influence to the variance of M values (to prevent false arc detections due to low-frequency weather changes), calculated M values can be fed to another functional block for SIC evaluation (second stage), with period K'. The resulting M' values, from the second stage of SIC evaluation, can be used to quantify measure of disorder of the previously calculated M values (from the first stage of the SIC evaluation). Fig. 5 illustrates the M' values calculated from the M values of signals s_1, s_2, and s_3 from Fig. 4, with period $K' = 10$ and $q' = 2$.

As can be seen from Figs. 4 and 5, when M and M' are calculated for periodic signals like s_1 and s_2, their variance is small (M relatively small and M' very small) compared to the case of the signal with added pink noise (signal s_3). In the case of signal s_3, chaotic behavior of M manifests through the appearance of high pulses in M' values. It is important to note that even with the arbitrary harmonic content of signal s_1, its M values remain equally ordered. The M values will remain equally ordered as long as the signal s_1 behaves according to the same pattern. This "patterned" behavior is characteristic for the PV system in normal (unfaulted) operating regimes [28]. Conversely, when the SEA is present, the corresponding M values will be disordered (as in the case of signal s_3, shown in Fig. 4) and the M' will assume high values. This property is used to establish a criterion for the SEA detection in the proposed detection algorithm.

The values for K and K' need to be chosen such that the corresponding periods are smaller than periods of changes of operating regimes. For example, if a current is sampled at 10 kHz, and K and K' are set to be 100 and 10, the periods on which M and M' values are calculated are 0.01, and 0.001 s. Since the second stage is used for the detection, and because the maximum rate of changes in the operating conditions caused by clouds or wind induced vibrations is significantly below 100 Hz [18], no risk of false trip is expected. This is confirmed in Fig. 5, where the M' values of the synthetic signal s_2 are presented.

B. Digital Implementation of the Proposed Algorithm

For SIC evaluations according to (5), the K samples are stored in a FIFO circular buffer. An index keeps track of the current

position in the buffer, in which the old value x_{old} is replaced with the new value x_{new}. The $M[i]$ value is calculated for each new sample, using simpler expression obtained from (5)

$$M\left[i\right] = \frac{\sum_{i=1}^{K} x\left[i\right]^{2q}}{\left(\sum_{j=1}^{K} x\left[j\right]^{2}\right)^{q}} \tag{6}$$

i.e.

$$M\left[i\right] = \frac{A\left[i\right]}{B\left[i\right]^{q}} \tag{7}$$

where

$$\begin{aligned} A\left[i\right] &= \sum_{i=1}^{K} x\left[i\right]^{2q} \\ B\left[i\right] &= \sum_{j=1}^{K} x\left[j\right]^{2}. \end{aligned} \tag{8}$$

By using x_{old} and x_{new}, $A[i]$ and $B[i]$ can be calculated in recursive form as

$$\begin{aligned} A\left[i\right] &= A\left[i-1\right] + x_{\mathrm{new}}^{2q} - x_{\mathrm{old}}^{2q} \\ B\left[i\right] &= B\left[i-1\right] + x_{\mathrm{new}}^{2} - x_{\mathrm{old}}^{2}. \end{aligned} \tag{9}$$

Calculations of $A[i]$ and $B[i]$ by using (9) and $M[i]$ by using (7) are easy to implement on a microcontroller. However, successive calculations of (9) can lead to numerical instability due to accumulated rounding error that can appear after a large number of arithmetical operations. To overcome this problem, the correct values of $A[i]$ and $B[i]$ should be calculated by using (8) and should replace the values calculated by (9) after a certain number of iterations. The correct values of $A[i]$ and $B[i]$ can be calculated at every Kth sample (at the end of every circular buffer cycle). First, the $A_2[i]$ and $B_2[i]$ are computed in parallel with (9) at every sample, such that

$$\begin{aligned} A_2\left[i\right] &= A_2\left[i-1\right] + x_{\mathrm{new}}^{2q} \\ B_2\left[i\right] &= B_2\left[i-1\right] + x_{\mathrm{new}}^{2}. \end{aligned} \tag{10}$$

Then, after every Kth sample, the values of $A[i]$ and $B[i]$ [calculated by (9)] are overwritten with $A_2[i]$ and $B_2[i]$ to cancel the accumulated rounding error, and $A_2[i]$ and $B_2[i]$ are set to zero.

The flowchart of the proposed detection algorithm is presented in Fig. 6. At the algorithm initialization, before the interrupt routine is enabled, all flag values are set to zero, and buffers are filled with random positive values. In the interrupt routine, a signal from the A/D converter is fed to the first block for calculation of $M[i]$. $M[i]$ values are then fed to another block for SIC evaluation, and the values of $M'[i]$ are obtained. The K and K' were set to 100 and 10, respectively, and the q and q' were set to 4 and 2, respectively. The definition and physical meaning of parameter q can be found in [24]. From the purely mathematical point of view, we can conclude that selection of $q > 1$ results in heavier impact of the samples with the higher amplitude on the overall calculation of signal entropy. Therefore, selection of $q > 1$ is quite logical. Selection of too big q could shorten the detection time, but it would increase the sensitivity to outliers

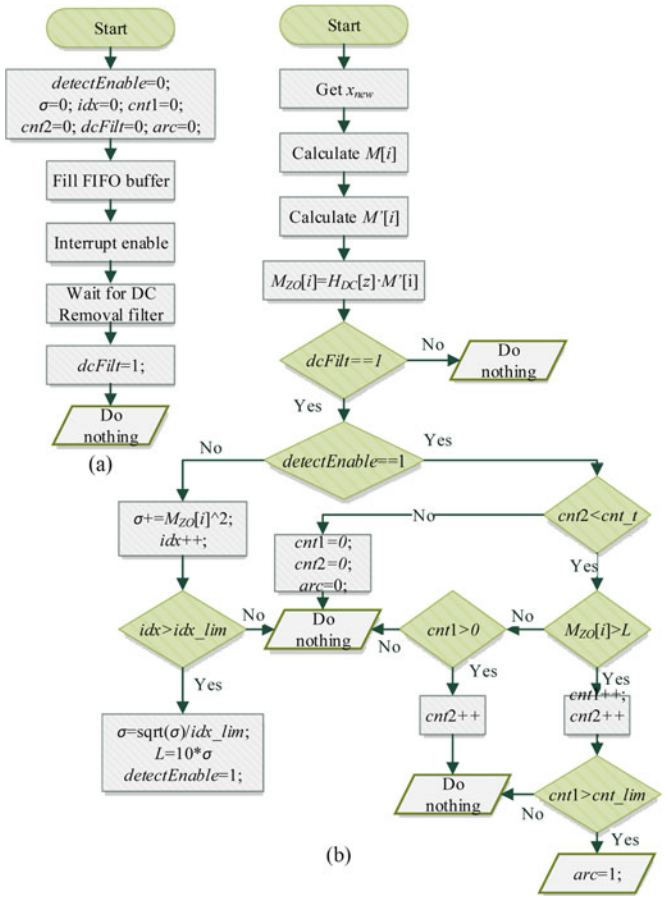

Fig. 6. Flowchart of the proposed algorithm. (a) Main function. (b) Interrupt routine.

(that could be result of noise). Additional issues are practical computational load and maximal values of numbers which can be represented in microcontroller. Having all that in mind, it seemed reasonable to select natural numbers which are in the range from 2 to 6 as q values (and that was later confirmed by experiments). If values of q' and q are chosen as 2 and 4, values of $x[i]^{2q'}$ and $x[i]^{2q}$ can be calculated with two and three multiplications, respectively. This requires less computational effort than calculation of powers of other real numbers from the mentioned range.

After the $M'[i]$ calculation, its dc offset is removed with the HPF, and the values $M_{\mathrm{ZO}}[i]$ are obtained. The transfer function of the first-order HPF in discrete domain can be written as

$$H_{\mathrm{DC}}\left[z\right] = \frac{1 - z^{-1}}{1 - \alpha z^{-1}}. \tag{11}$$

The value of α from (11) needs to be chosen such that the change in offset of $M'[i]$ is removed fast enough, and that variations caused by the SEA induced noise are not affected by the filtering. Since the offset is mainly caused by the nature of its calculation (and virtually does not depend on the change of the operating conditions), it does not need to be quickly removed. In this implementation, α is set to 0.99 which results in first-order HPF with cut-off frequency $f_c \approx 16$ Hz.

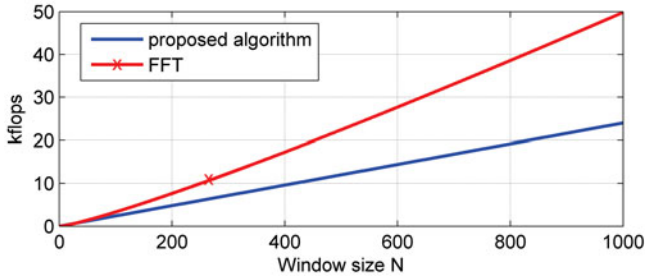

Fig. 7. Comparison of computational complexity (in kilo flops) between FFT from [29] and the proposed algorithm.

After the initialization in the main function and the calculation of the $M_{ZO}[i]$ values, the algorithm waits for the HPF to bring the offset to zero. Value *dcFilt* is used to delay threshold calculation until the dc component is removed (*dcFilt* is set to 1 after the dc component is filtered out). The algorithm then calculates standard deviation (σ) of signal $M_{ZO}[i]$, which is used to create a threshold (L) for SEA detection. Since the $M_{ZO}[i]$ has no dc component, the σ can be approximately calculated as a root mean square of certain number of samples. Based on the analysis of the large number of measurements, the threshold limit L is set to 10σ. This value proved to be large enough to prevent false detection, but at the same time small enough to detect even shortest tested SEA. Other similar values (e.g., 15σ or 20σ) can be used as well. After the threshold limit L is set, a flag *detectEnable* is set to 1 and algorithm is ready for operation. When an SEA occurs, the value $M_{ZO}[i]$ crosses the threshold limit L and algorithm starts to count samples for which $M_{ZO}[i]$ is higher than L in the time period set by *cnt_t*. If the number of those samples (*cnt*1) is larger than *cnt_lim* (in our case *cnt_lim* was set to 50), arc detection is signalized. The guaranteed detection time of the proposed technique is defined with variables *cnt_t*, *K,* and *K*′. If the *cnt_t*, *K,* and *K*′ are set to 5000, 100, and 10 and if the sample rate is 10 kHz, the guaranteed detection time is set to 0.511 s.

C. Algorithm Processing Power Requirements

As stated before, the calculation of $M[i]$ and $M'[i]$ values is done by using (7), (9), and (10). In order to calculate the values $M'[i]$, when q' is set to 2, the values of x^2_{new}, x^2_{old}, x^4_{old}, x^4_{new} are required. These four values can be calculated by using four multiplications: two to get x^2_{new} and x^2_{old} and two more to calculate x^4_{old} and x^4_{new}. In (9) and (10), four additions and two subtractions are required. The M'[i] is finally calculated by using one division according to (7). In order to calculate the values $M[i]$, when q is set to 4, the values of x^2_{new}, x^2_{old}, x^8_{old}, x^8_{new} are required. These values can be calculated by using six multiplications: two to get x^2_{new}, and x^2_{old}, and four more to get x^8_{old} and x^8_{new} ($x^4_{\text{old}} = x^2_{\text{old}} \cdot x^2_{\text{old}}, x^8_{\text{old}} = x^4_{\text{old}} \cdot x^4_{\text{old}}$). Number of additions, subtractions, and divisions is the same as in the case of $M'[i]$. Therefore, in order to calculate $M[i]$ and $M'[i]$ values on a window of size N, $24N$ flops are required. As an illustration, Fig. 7 presents the computational complexity of the fast Fourier transform (FFT) algorithm proposed in [29] and the algorithm proposed here. The FFT from [29] requires approximately $5N\log_2 N$ flops per window.

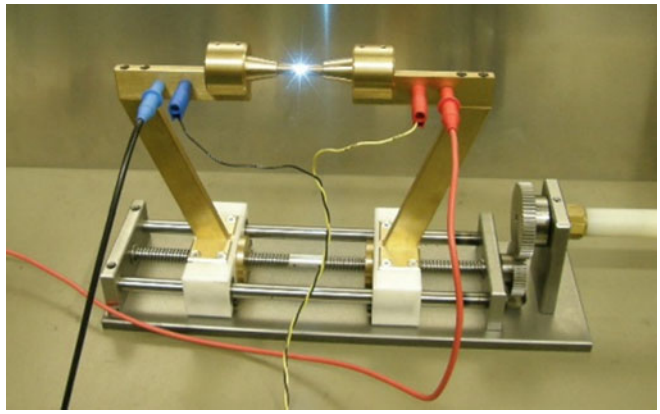

Fig. 8. Custom-made arc generator.

D. Briefly About Arcs Used for Testing of the Algorithm

As described in further text, there were two groups of tests of the algorithm: on prerecorded data and after implementation on the detector prototype. The custom made arc-generating device is presented in Fig. 8.

In both cases, the electric arc was generated by manually pulling apart the two cylindrical copper electrodes of 8 mm diameter. During all the experiments (i.e., during the collection of data used for simulations and during the experimental verification), the main focus was on short arcs. In most cases, the arc length was around 1 mm or less. The short arcs are assumed as the most realistic case (loosened contacts at the PV panel, in the junction boxes, etc.) and also as the case in which the arc fault is hardest to detect. The detector operation was experimentally verified on sustained arcs as well.

More details on arc characteristics can be found in [9] and [12]. A sustained arc results if the energy produced inside the arc is higher than energy loss during arcing [9]. The sustainability of an arc depends on many factors, such as size of electrodes, air gap length, etc. According to [3], it is difficult to generate arc faults in the dc circuit between PV panels and the inverter if the length of a PV string is not sufficient. The experimental study of dc arc characteristics is presented in [12], where the influence of arc length, electrodes diameter, dc-source voltage, and arc current level is studied in detail.

E. Application of the Proposed Detection Algorithm on the Prerecorded Data From the System With the PV Panel Simulator and the Commercial Inverter

The simulations of the proposed detection algorithm are performed on a set of signals which are recorded with a 100-kHz sampling frequency in a system consisting of a TopCon PV panel simulator with the SASControl software and a SOLIVIA 3.3 TR PV inverter. The PV panel simulator current is recorded on the secondary of a current transformer, and, therefore, it does not contain a dc component of the PV current. A 50-μH inductor is connected in series with the inverter input terminals in

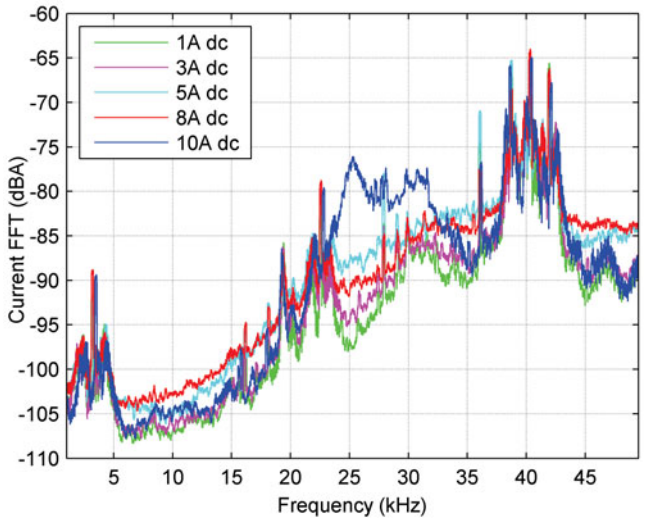

Fig. 9. Inverter noise signatures at five different loads, smoothed with a 160-Hz sliding window.

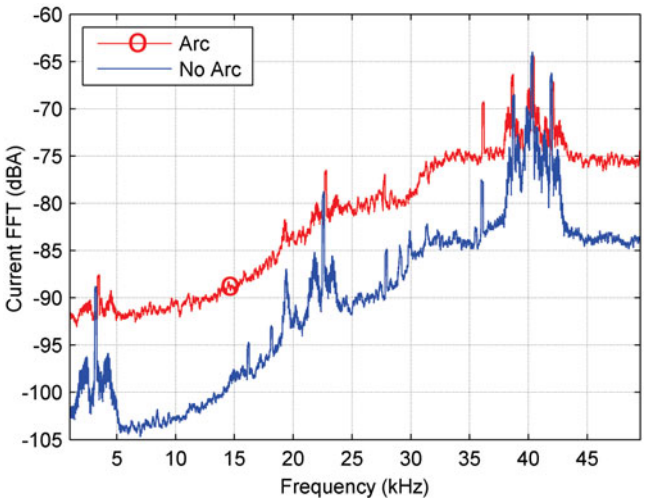

Fig. 10. Inverter noise signatures of unfaulted and faulted (with SEA) operating regimes, both at input current of 8 A, smoothed with a 160-Hz sliding window.

order to simulate the filtering effect of dc cables. This inductance is approximate to the inductance of the two 100-m-long typical solar 2.5 mm^2 single jacket cables laid in flat formation. The simulator current is recorded for five different operating conditions with current ranging from 1 to 10 A. Fig. 9 depicts the corresponding inverter noise signatures, smoothed with a 160-Hz sliding window.

As can be seen from Fig. 9, the noise signature at 10 A is significantly different from other noise signatures in the frequency range from 23 to 35 kHz. The variations of the inverter noise signature with the load are pointed out in [28]. Those variations are caused by inverter control and commutation transients. Therefore, the arc detection algorithms which monitor certain range of PV panel (or string) current spectrum would have to be carefully calibrated (in the case from Fig. 9 the frequency range from 23 to 35 kHz should be avoided) in order to be able to detect an arc under all load conditions. Fig. 10 shows

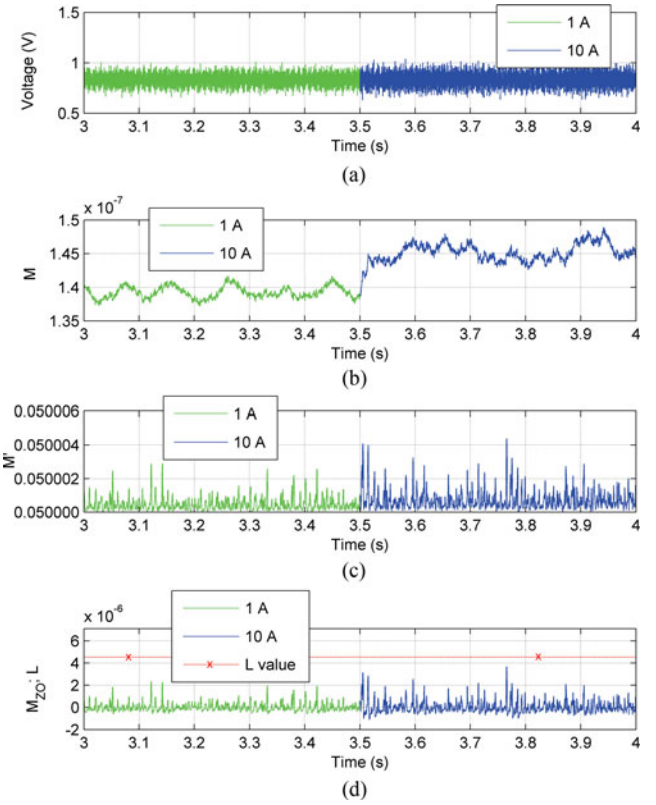

Fig. 11. Algorithm operation in case with no SEA, but with abrupt change of PV current from 1 to 10 A at 3.5 s: (a) Output voltage of the current measurement circuit, (b) M values, (c) M' values, and (d) M_{ZO} values and limit L.

that the noise caused by SEA superimposes to the inverter noise signature from an unfaulted operating regime, which is in agreement with the results from [28].

For the implementation of the proposed algorithm, the prerecorded current signals were resampled to 10 kHz by taking every tenth sample of the originally recorded data, and K and K' were set to 100 and 10, respectively. In order to test the algorithm's resistivity to nuisance trips, a test signal is formed by concatenating the waveform recorded at 1-A PV panel simulator current and the waveform recorded at 10-A PV panel simulator current, as shown in Fig. 11. The combination of these two waveforms is chosen because their noise signatures differs the most from one another (see Fig. 9). The current measurement circuit's output voltage is shown in Fig. 11(a), and the M and M' values are shown in Fig. 11(b) and (c), respectively. The measurement circuit consisted of the current transformer and the high-pass filter (details are given in Section IV) which was connected to the current transformer's secondary. The primary of the current transformer has had one turn of the conductor carrying the PV string current. Therefore, as shown in Fig. 11(a), the measurement circuit's output voltage is not proportional to the dc component of the PV string current. The threshold limit L and the M_{ZO} values are shown together in Fig. 11(d). The transition from 1-A signal to 10-A signal occurs at 3.5 s. As shown in Fig. 11, the M changes noticeably after the transition [see Fig. 11(b)], but the change of the M' is practically insignificant [see Fig. 11(c)]. The threshold limit shown in Fig. 11(d) is

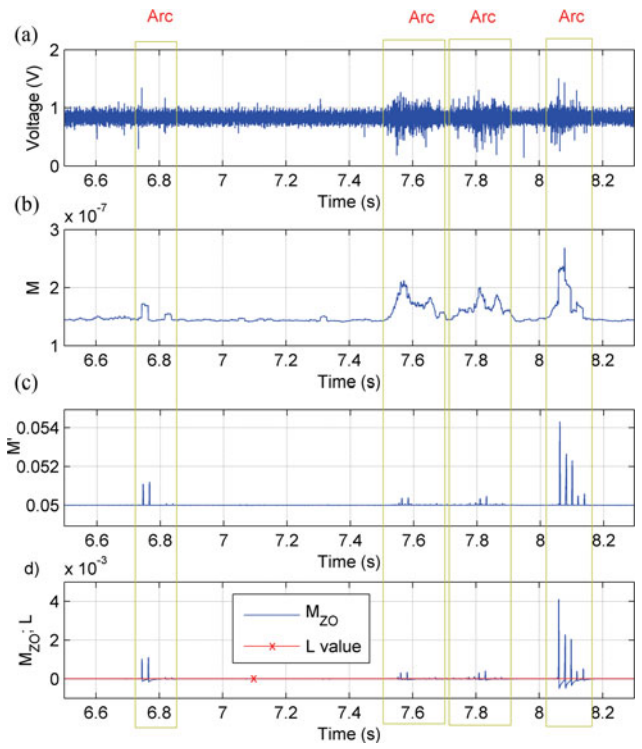

Fig. 12. Algorithm operation in case of multiple SEA occurrences at 8-A current: (a) Output voltage of the current measurement circuit, (b) M values, (c) M' values, and (d) M_{ZO} values with limit L.

set to $L = 10 \cdot \sigma$, where σ is calculated on the 1-A signal, using the algorithm illustrated in Fig. 6.

Fig. 12 depicts the algorithm operation when multiple SEAs occur, at 8-A input current. As shown in Fig. 12, the calculated M values increase when the SEA occurs, and deviations of M_{ZO} values become up to 800 times larger than the calculated value of L, i.e., 8000 times larger than the determined standard deviation. This enables user to set very high threshold limits (of order ten times the standard deviation, or more), and, thus, increase the algorithm robustness and eliminate potential nuisance trips. The calculated values of $M_{ZO}[i]$ are shown in Fig. 12, along with the threshold value L from Fig. 11(d). A variable *arc* is set to 1 when the SEA is detected. For this test, *arc* and *cnt*1 variables are intentionally reset to zero 50 ms after they have been set, in order to get better understanding of the algorithm operation and of the time needed for detection in case of multiple or sustained arcs. Areas with limit crossings and counter of limit crossings (*cnt*1), from which the performance of the algorithm can be tracked, are presented on Fig. 13. The *cnt_lim* was set to 50.

F. Problem of Initialization During SEA—The Auxiliary Detection Algorithm

Although a dynamic threshold limit setting seems like a logical approach to the arc-fault detection, the problem could potentially arise in the case when an arc fault exists during the algorithm initialization stage. In that case, the established threshold limit could be too high and any subsequent arc fault could go undetected. In order to resolve this problem, an auxiliary detection algorithm which does not rely on "learning" parameters is

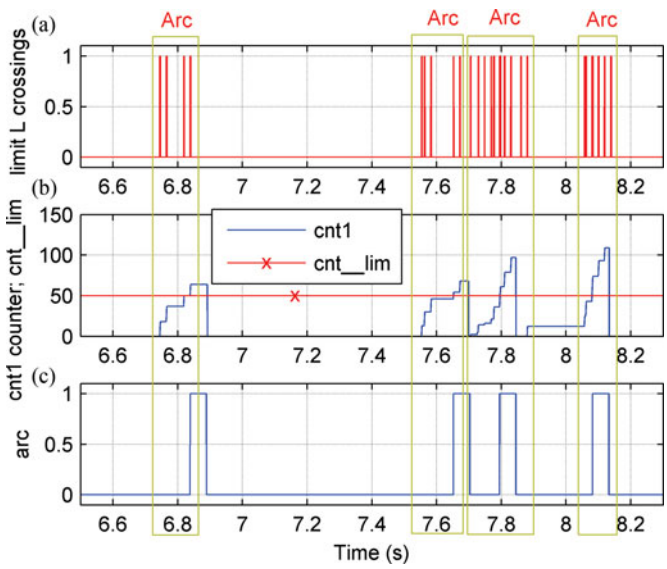

Fig. 13. Internal parameters of the proposed algorithm in case of multiple SEA occurrences at 8-A current: (a) Intervals where the variable M_{ZO} is higher than the limit L, (b) counter of those limit crossings (*cnt*1) and triggering limit (*cnt_lim* = 50), and (c) variable *arc*.

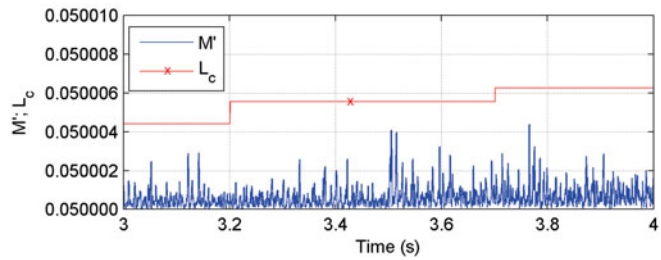

Fig. 14. M' values and limit value L_c calculated every 0.5 s in the case of a step change of PV current at 3.5 s.

introduced. The auxiliary algorithm utilizes the pulsing nature of the M' values during arcing period. Namely, the M' values can be processed in successive windows, on which the statistical properties of M' (e.g., mean value and standard deviation) can be calculated. As an illustration, we can analyze the signals from the current measurement circuit, which are presented in Fig. 11 (no arc operation) and Fig. 12(a) (multiple SEAs occur).

The M' values from Fig. 11 and the calculated limit L_c are presented in Fig. 14. The limit L_c is calculated as a sum of the mean value of M' and the standard deviation of M' multiplied by 10. The calculations are performed every 0.5 s. As can be seen from Fig. 14, there are no crossings of the limit L_c.

The same method is used in the case of SEA from data presented in Fig. 12(a) and the result is presented in Fig. 15(a). By looking at the Fig. 15(a), it can be concluded that there is a significant rise in the limit L_c in those 0.5-s windows where the arc is present. This is because of the high-amplitude pulses which increase the mean value and the standard deviation of the M'. However, despite the rise of the limit L_c, there were some limit crossings in those 0.5-s windows with the SEA. The auxiliary detection algorithm can be established as follows. The number of samples with values higher than limit L_c is counted in each 0.5-s window, and if in each of two consecutive 0.5-s

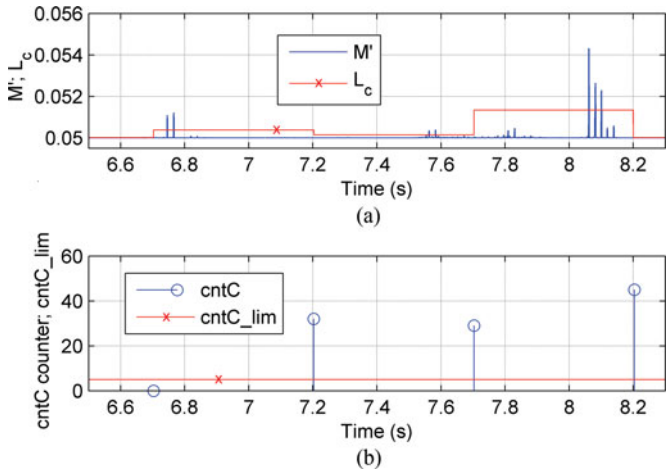

Fig. 15. (a) M' values and limit value L_c calculated every 0.5 s in the case of the SEA, and (b) internal parameters *cntC* and *cntC_lim* of the auxiliary algorithm.

windows, the number of those samples becomes higher than the predefined value (*cntC_lim*), arc detection will be signalized. Since this algorithm does not need any previous initialization, but does the independent calculations every 0.5 s, it can be used to detect the arc during the commissioning procedure. The internal parameters of the algorithm are presented in Fig. 15(b), where *cntC* variable, calculated at the end of each window, represents the number of samples with values higher than L_c. The *cntC_lim* was set to 5. In most cases, this detection criterion is slower from the one proposed in Section III-A, and, therefore, our recommendation is to use this criterion only during the commissioning of the system. The guaranteed detection time of this method, for the sustained arc, is 1.5 s, which equals three windows of 0.5 s. This is because two consecutive windows with SEA are needed to guarantee the detection (the threshold in each of the windows needs to be exceeded). The existence of SEA only in a part of a window may be insufficient to exceed the limit.

IV. Experimental Evaluation of the Realized Detector

The schematic representation of the experimental setup is shown in Fig. 16, and a part of the experimental setup is shown in Fig. 17. The PV string was located outside the building and is not shown in the figure. The arc generator was also separated from the rest of the setup in order to mitigate the influence of the arc-generated noise to the communication with the DSP.

The realized detector prototype consists of a current transformer wound on a toroid core T106-52 from micrometals, with 1 turn on the primary and 130 turns on the secondary. A first-order high-pass filter (made with precision operational amplifier OPA376) with 1-kHz crossover frequency was connected to the transformer secondary. The output of the filter was fed to the TMS320F28335 experimenter kit DSP control card.

The detector is tested in a dc circuit of the grid-connected PV system, which consists of 6 PV panels (first solar ZDNY-235P60) connected in series, with total rated power of 1.41 kW,

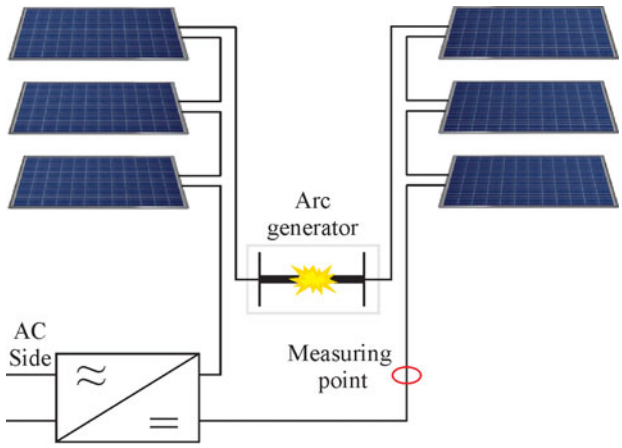

Fig. 16. Schematic representation of the experimental setup.

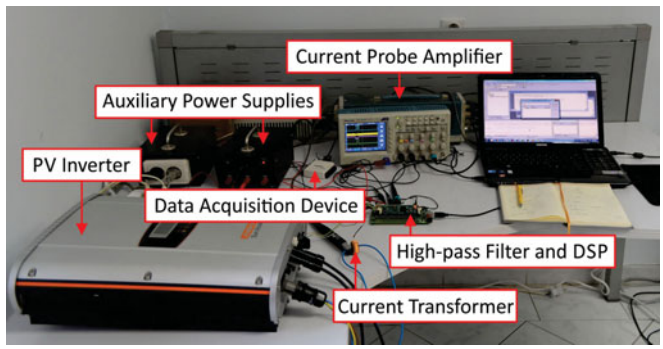

Fig. 17. Part of the experimental setup with the detector prototype in operation.

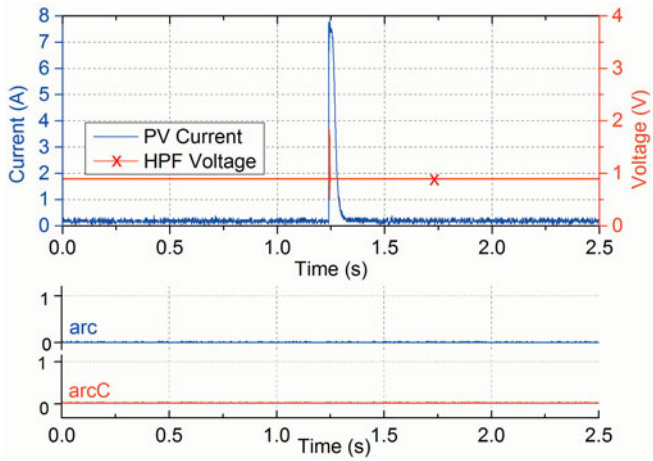

Fig. 18. Detectors' response to a PV current spike at the inverter switch-on instant.

and a 1.6 kW single-phase SG 1K5TL-31 PV inverter. The electric arc was generated by manually pulling apart the two cylindrical copper electrodes of 8 mm diameter. The measured current signal was sampled at 10 kHz, and K, K', q, and q' were set to 100, 10, 4, and 2, respectively, as determined in the previous section. The detector parameters were not additionally adjusted for the PV system in which the tests were performed.

In all analyzed cases, measurements were made with four channel oscilloscope TDS2024C. In order to increase the read-

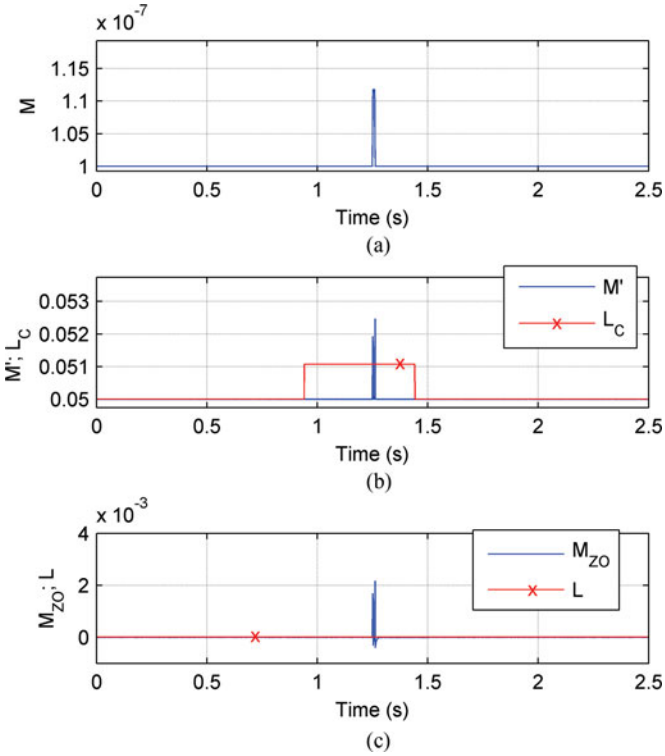

Fig. 19. Main and the auxiliary algorithm operation in case of a PV current spike at the inverter switch-on instant: (a) M values. (b) M' values and limit L_C. (c) M_{ZO} values and limit L.

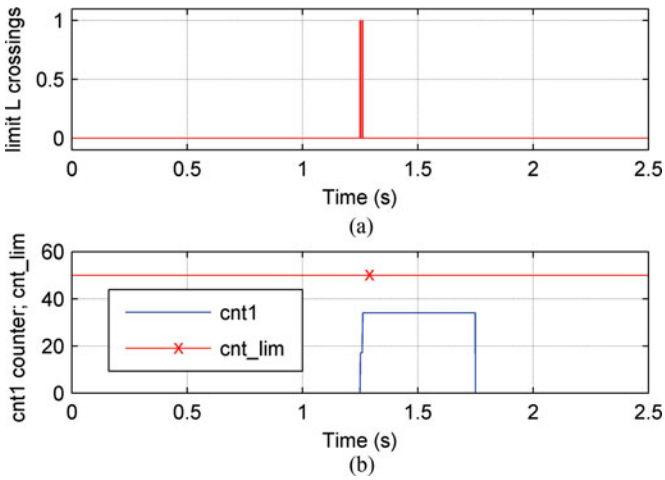

Fig. 20. Internal parameters of the main algorithm in case of a PV current spike at the inverter switch-on instant: (a) Intervals when variable M_{ZO} is higher than limit L. (b) Counter of those limit crossings (*cnt*1) and triggering limit (*cnt_lim*).

ability of the experimentally obtained waveforms, the experimental data were transferred from oscilloscope as comma-separated values and plotted in MATLAB. During all the experiments, the output voltage of HPF was logged with the National Instruments USB 6009 data acquisition device. The internal parameters of the algorithm, which are reconstructed from the measurements of the HPF output voltage, were shown after the figures of detector response.

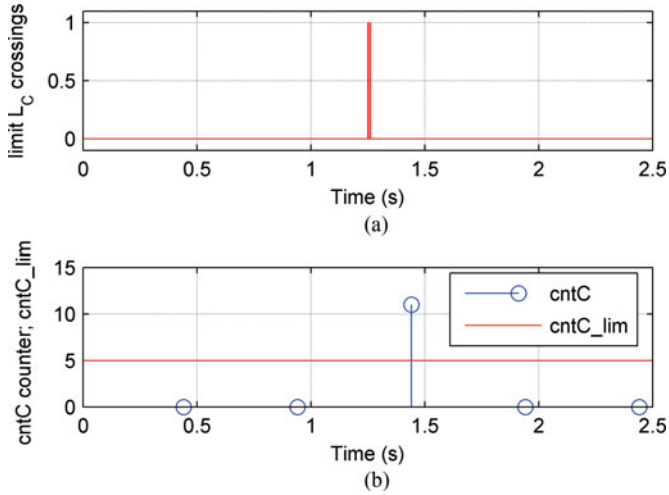

Fig. 21. Internal parameters of the auxiliary algorithm in case of a PV current spike at the inverter switch-on instant: (a) Limit L_C crossings, and (b) internal parameters *cntC* and *cntC_lim* of the auxiliary algorithm.

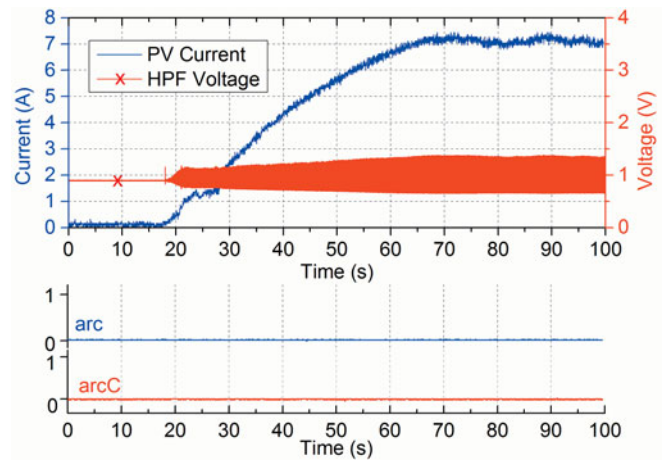

Fig. 22. Detectors' response during a MPPT operation.

In all performed tests, both detection algorithms (main and auxiliary) are tested at the same time. However, as previously suggested, the auxiliary detector should be active only during the commissioning stage. In order to test the detectors' resistivity to nuisance trips, the following two cases are analyzed: a normal inverter turn on with the active maximum power point tracking (MPPT), and a step change of the PV panel current during the inverter operation. The following signals were monitored: PV current, HPF output voltage, and the voltages of the DSP output pins that represent outputs of the both detection criteria (variables *arc* and *arcC*).

The testing procedure was as following. After the inverter is switched ON, it requires a few minutes to synchronize with grid. During this process, no power flows from the PV string. In order to avoid the calculation of limit L at the zero PV current (during the synchronization), the limit L was calculated after this synchronization period.

In the first test case (see Fig. 18), a large spike in PV current, and fast transient of HPF output voltage can be observed at the instant when the inverter was switched ON. Both detectors did

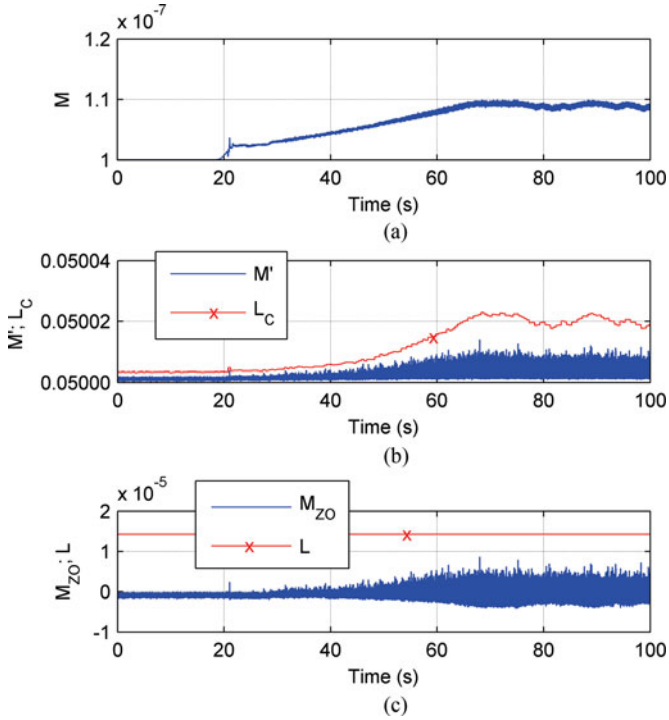

Fig. 23. Main and the auxiliary algorithm operation during the MPPT action: (a) M values. (b) M' values. (c) M_{ZO} values and limit L.

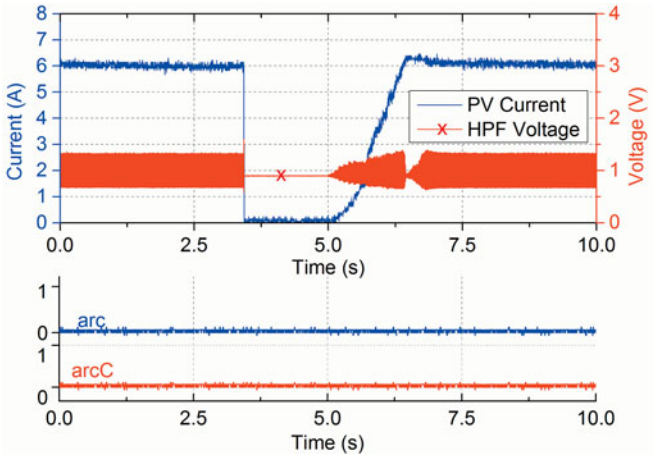

Fig. 24. Detectors' response to a step change of the PV current.

not falsely trip during this transient. The internal parameters of the algorithms are shown on Figs. 19–21. Values of M, M', and M_{ZO} increase during the transient, but the period of transient is very short. Parameter that indicate SEA presence (*cnt*) does not reach triggering limit [see Fig. 20(b)], and *arcC* does not trigger because limit L_C crossings [see Fig. 21(a)] occurs only at one 0.5-s window [see Fig. 21(b)].

In case when the turn on appears long time (few minutes) after previous turn off, the MPPT is activated after synchronizing. A slow current rise due to the MPPT action can be observed in Fig. 22. As illustrated in [28], the inverter noise signature changes significantly during this startup procedure. This can be also seen on the HPF output voltage waveform.

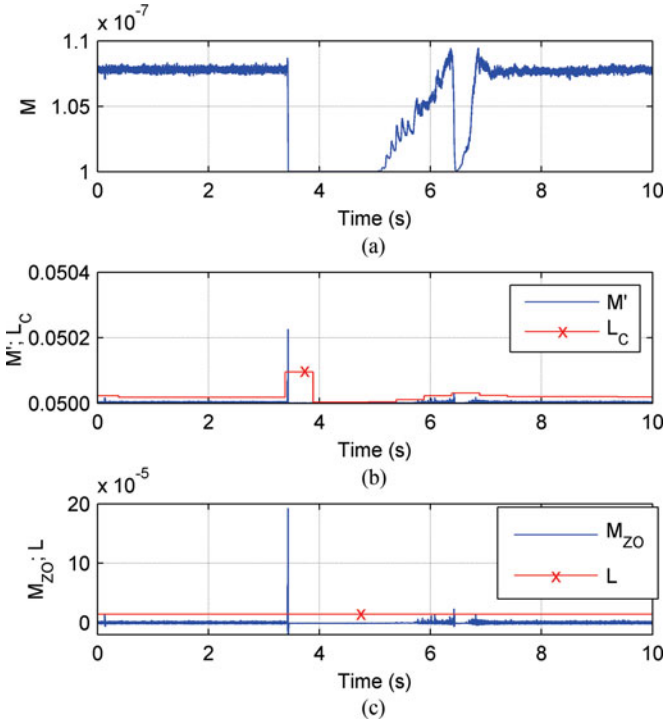

Fig. 25. Main and the auxiliary algorithm operation in case of a step change of the PV current: (a) M values. (b) M' values and limit L_C. (c) M_{ZO} values and limit L.

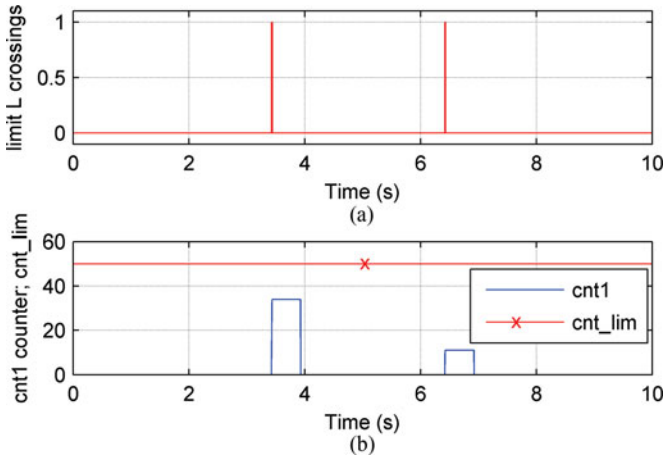

Fig. 26. Internal parameters of the main algorithm in case of a step change of the PV current: (a) Intervals when variable M_{ZO} is higher than limit L, and (b) counter of those limit crossings (*cnt*1) and triggering limit (*cnt_lim*).

As can be seen from Fig. 22, both detectors did not falsely trip despite the disturbances in the PV current during the startup procedure. The internal parameters of the algorithms are shown in Fig. 23. M value, variations of M', and M_{ZO} increase slowly during the startup procedure, but no crossings of limits L and L_C can be observed.

For the second test, a step change in the PV current is introduced by turning the inverter off and then on shortly after. The inverter's MPP tracker remembers the last maximum power point for some short time, and if it was switched ON again by that time, the operating point is set to the remembered value. As shown in Fig. 24, both detectors did not falsely trip despite the

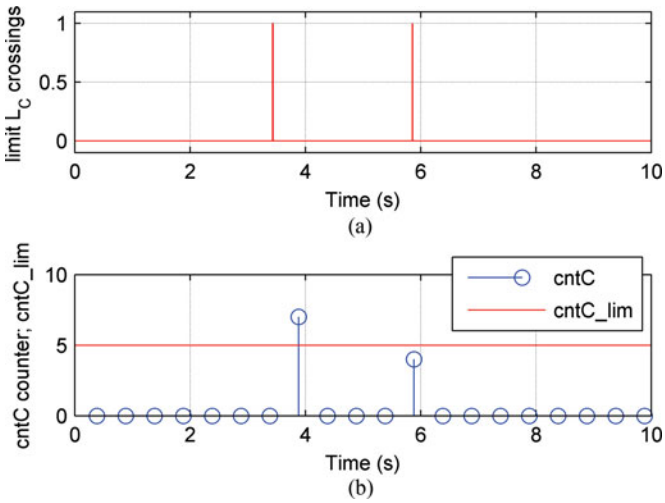

Fig. 27. Internal parameters of the auxiliary algorithm in case of a step change of the PV current: (a) Limit L_C crossings, and (b) internal parameters *cntC* and *cntC_lim* of the auxiliary algorithm.

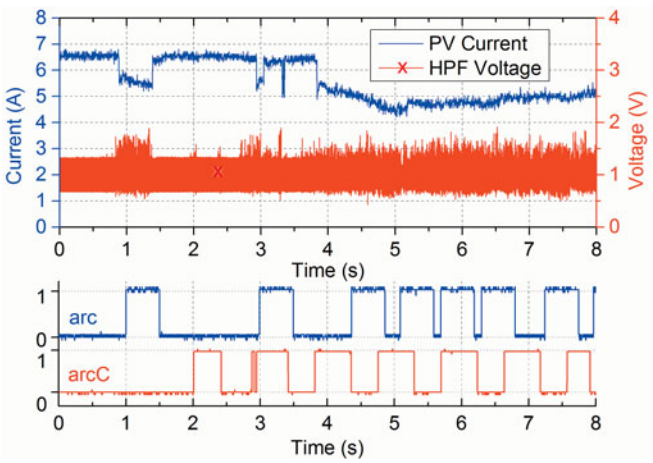

Fig. 28. Detectors' response to a short-term arc followed by the series of spark arcs and sustained arc, at output power of 940 W.

introduced PV current step change. The internal parameters of the algorithms are shown on Figs. 25–27. As can be seen from Fig. 25(b) and (c), some limit crossings appear after the current step change [see Figs. 26(a) and 27(a)], but their number and duration is small to cause false detection [see Figs. 26(b) and 27(b)].

On the other hand, the SEA was successfully detected every time it occurred. The tests were performed for different arc types: spark arcs, short-term arcs, and sustained arcs. It was difficult to generate sustained arcs that last longer than 5 s (ignition difficulties in the smaller system are also reported in [3]). The tests showed that algorithm detected arcs of all three types.

The detector's response to a short-term arc, followed by a series of spark arcs and the sustained arc, at output power of 940 W (power is read from the inverter display), is shown in Fig. 28. The time needed for the algorithm to detect the each SEA was less than the guaranteed (with the parameters set as described in the introduction of Ch. IV, the guaranteed time is

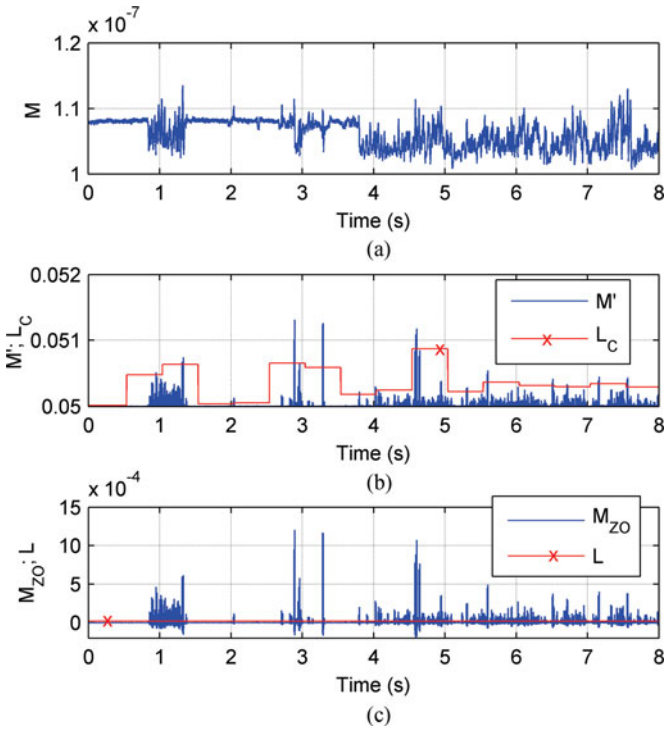

Fig. 29. Main and the auxiliary algorithm operation in case of a short-term arc followed by the series of spark arcs and sustained arc: (a) M values, (b) M' values and limit L_C, and (c) M_{ZO} values and limit L.

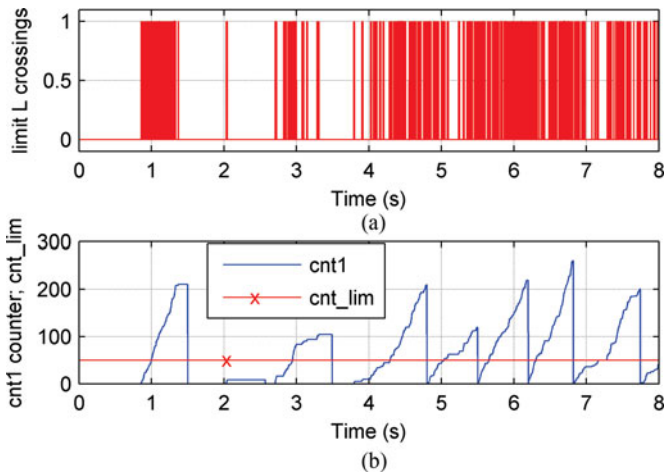

Fig. 30. Internal parameters of the main algorithm in case of a short-term arc, followed by the series of spark arcs and sustained arc: (a) Intervals when variable M_{ZO} is higher than limit L, and (b) counter of those limit crossings (*cnt*1) and triggering limit (*cnt_lim*).

0.511 s for *arc* variable, and 1.5 s for *arcC* variable). The actual detection time depends on the characteristics of the arc and the moment of its appearance in respect to the calculation window. Typical detection time achieved in the performed experiments was around 200 ms for *arc* variable and 800 ms for *arcC* variable.

The internal parameters of the algorithms are shown on Figs. 29–31. During arcing periods, M value changes stochastically and M' and M_{ZO} values increase significantly (see Fig. 29), causing frequent multiple crossings of limits L and L_C [see Figs. 30(a) and 31(a)], and the arcs are detected.

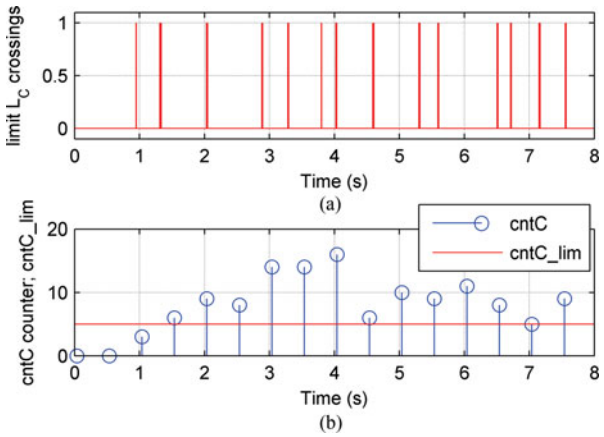

Fig. 31. Internal parameters of the auxiliary algorithm in case of a short-term arc, followed by the series of spark arcs and sustained arc: (a) Limit L_C crossings, and (b) internal parameters *cntC* and *cntC_lim* of the auxiliary algorithm.

V. Conclusion

This paper has presented a series arc-fault detection algorithm for PV systems, based on monitoring of the PV panel current entropy. Based on the calculated entropy of the PV current, the algorithm is able to differentiate an arc state (when the current variations are chaotic) from a no-arc state (when the current variations are ordered). The algorithm operates on a plug-and-play principle, and it automatically adapts to the conditions and sets the threshold value for the proper SEA detection. When compared to the arc-fault detection methods that are based on outlier detection rules (like 3-sigma, Hampel identifier, and Boxplot), which also do not require previous training data, triggering limits in the proposed algorithm can be set much higher. This can greatly reduce false tripping.

The main advantage of the proposed algorithm, compared to the algorithms that are based on the frequency spectrum monitoring, is that the noise signature of the target PV system, as well as the manual calibration of the detector's parameters are not required for its proper operation. The proposed algorithm is also less computationally expensive than FFT-based algorithms, so it can reduce the cost of the overall product.

In this paper, the operation of the detection algorithm was simulated on a set of prerecorded data from the commercial single phase 3.3-kW inverter and PV panel simulator, taken at five different loads. The detector prototype was then built and its operation was experimentally verified in a grid-connected 1.6-kW PV system, without any prior analysis of the target PV system or any additional algorithm parameter adjustments. Both the simulations and the experiments have confirmed a proper operation of the detector without nuisance trips. During experimental evaluation, input signal of detector prototype is recorded and internal parameters of algorithm are reconstructed on computer. Analysis of internal parameters revealed modest sensitivity to current step change and large current spike during turn on transient, and confirmed efficiency in SEA detection.

Acknowledgment

The authors would like to thank Delta Energy Systems GmbH Company, Germany, for the experimental data obtained from PV panel simulator and commercial inverter, and to Prof. Z. Djurisic from the School of Electrical Engineering, University of Belgrade, for kindly providing the access to the PV system on which the developed detector prototype was tested.

References

[1] (2015, May). Global market outlook for photovoltaics 2015-2019. SolarPower Europe, Brussels, Belgium. [Online]. Available: http://solarpowereurope.org/insights/global-market-outlook/

[2] J. Yuventi, "DC electric arc-flash hazard-risk evaluations for photovoltaic systems," *IEEE Trans. Power Del.*, vol. 29, no. 1, pp. 161–167, Feb.xbrk 2014.

[3] J. Johnson, M. Montoya, S. McCalmont, G. Katzir, F. Fuks, J. Earle, A. Fresquez, S. Gonzalez, and J. Granata, "Differentiating series and parallel photovoltaic arc-faults," presented at the IEEE 38th Photovoltaic Spec. Conf., Austin, TX, USA, Jun. 4, 2012.

[4] P. Jackson, "Target roof PV fire of 4-5-09," Development Services/Building Department, City of Bakersfield, CA, Memorandum, 4-29-2009, Apr. 29, 2009.

[5] "National electrical code 2014 Handbook," 13th ed: National Fire Protection Associations, Quincy, MA, USA, 2013.

[6] C. Strobl and P. Meckler, "Arc faults in photovoltaic systems," in *Proc. IEEE Electr. Contacts Conf.*, 2010, pp. 1–7.

[7] N. Hadziefendic, M. Kostic, and Z. Radakovic, "Detection of series arcing in low voltage electrical installations," *Eur. Trans. Electr. Power*, vol. 19, pp. 423–432, Feb. 2009.

[8] Y. Zhao, B. Lehman, J.-F. de Palma, J. Mosesian, and R. Lyons, "Fault analysis in solar PV arrays under: Low irradiance conditions and reverse connections," in *Proc. IEEE Photovoltaic Spec. Conf.*, 2011, pp. 2000–2005.

[9] M. K. Alam, F. Khan, J. Johnson, and J. Flicker, "A comprehensive review of catastrophic faults in PV arrays: Types, detection, and mitigation techniques," *IEEE J. Photovoltaics*, vol. 5, no. 3, pp. 982–997, May 2015.

[10] H. Haeberlin and M. Real, "Arc detector for remote detection of dangerous arcs on the DC side of PV plants," in *Proc. 22nd Eur. Photovoltaic Sol. Energy Conf.*, 2007, pp 1–6.

[11] F. Schimpf and L. E. Norum, "Recognition of electric arcing in the DC-wiring of photovoltaic systems," in *Proc. IEEE Telecommun. Energy Conf.*, 2009, pp. 1–6.

[12] X. Yao, L. Herrera, S. C. Ji, K. Zou, and J. Wang, "Characteristic study and time-domain discrete-wavelet-transform based hybrid detection of series DC arc faults," *IEEE Trans. Power Electron.*, vol. 29, no. 6, pp. 3103–3115, Jun. 2014.

[13] Y. Zhao, B. Lehman, R. Ball, J. Mosesian, and J. F. de Palma, "Outlier detection rules for fault detection in solar photovoltaic arrays," in *Proc. IEEE 28th Annu. Appl. Power Electron. Conf. Expo.*, Mar. 17–21, 2013, pp. 2913–2920.

[14] C. E. Restrepo, "Arc fault detection and discrimination methods," in *Proc. IEEE Electr. Contacts Conf.*, 2007, pp. 115–122.

[15] J. Johnson, B. Pahl, C. Luebke, T. Pier, T. Miller, J. Strauch, S. Kuszmaul, and W. Bower, "Photovoltaic DC arc fault detector testing at Sandia National Laboratories," in *Proc. IEEE Photovoltaic Spec. Conf.*, 2011, pp. 3614–3619.

[16] J. Johnson, S. Kuszmaul, W. Bower, and D. Schoenwald, "Using PV module and line frequency response data to create robust arc fault detectors," in *Proc. 26th Eur. Photovoltaic Sol. Energy Conf.*, 2011, pp. 3745–3750.

[17] B. Novak. (Jul. 2012). Implementing arc detection in solar applications: Achieving compliance with the new UL 1699B standard. Texas Instruments, Dallas, TX, USA. [Online]. Available: http://www.ti.com/lit/wp/spry209/spry209.pdf

[18] J. Schmid, E. Kancsar, M. Drapalik, V. Schlosser, and G. Klinger, "A study of the current disturbance caused by wind induced vibrations of photovoltaic modules," presented at the Int. Conf. Renewable Energies Power Quality, Granada, Spain, Mar. 23–25, 2010.

[19] F. Reil, A. Sepanski, S. Raubach, M. Vosen, and E. Dietrich, "Comparison of different DC arc spectra; Derivation of proposals for the development of an international arc fault detector standard," in *Proc. IEEE Photovoltaic Spec. Conf.*, 2013, pp. 1589–1593.

[20] M. Jankovic and N. Rubens, "A new probabilistic approach to on-line learning in artificial neural networks," in *Proc. Appl. Math., Simul., Model. Conf.*, 2009, pp. 226–231.

[21] L. Wolf, "Learning using the Born rule," Massachusetts Inst. Technol., Cambridge, MA, USA, Tech. Rep. TR-2006-036, 2006.

[22] P. A. Meyer, *Quantum Probability for Probabilists*, 2nd ed. Berlin, Germany: Springer, 1995.
[23] M. K. Warmuth and D. Kuzmin, "Bayesian generalized probability calculus for density matrices," *J. Mach. Learn.*, vol. 78, nos. 1/2, pp. 63–101, 2009.
[24] C. Tsallis, "Possible generalization of Boltzmann-Gibbs statistics," *J. Statist. Phys.*, vol. 52, pp. 479–487, 1988.
[25] M. Jankovic, T. Gajic, and Z. Janda, "Simple method for rotor failure detection based on quantum entropy," in *Proc. 17th Int. Symp. Power Electron.*, 2013, paper no. T.3.6.
[26] M. V. Jankovic and N. Georgijevic, "Applications of probabilistic model based on joystick probability selector," in *Proc. IEEE Neural Netw. Conf.*, 2014, pp. 1028–1035.
[27] A. Kacar and M. Jankovic, "P1078: Early diagnostic criteria for Parkinson's disease," *J. Clin. Neurophysiol.*, vol. 125, pp. S335–S336, 2014.
[28] J. Johnson and J. Kang, "Arc-fault detector algorithm evaluation method utilizing prerecorded arcing signatures," in *Proc. IEEE Photovoltaic Spec. Conf.*, 2012, pp. 1378–1382.
[29] J. W. Cooley and J. W. Tukey, "An algorithm for the machine computation of the complex Fourier series," *Math. Comput.*, vol. 19, pp. 297–301, Apr. 1965.

Nikola L. Georgijevic received the B.S. and M.S. degrees in electrical engineering from the School of Electrical Engineering, University of Belgrade, Belgrade, Serbia, in 2011 and 2012, respectively, where he is currently working toward the Ph.D. degree in electrical engineering.

Since 2011, he has been a Research Assistant with the Electrical Engineering Institute Nikola Tesla, University of Belgrade. His research interests include digital signal processing, power quality, and power system stability.

Marko V. Jankovic (SM'09) was born in Sabac, Serbia, on February 19, 1968. He received the Graduate degree from the Faculty of Electrical Engineering, University of Belgrade, Belgrade, Serbia, in June 1990, and the master's and doctoral degrees, from the same university, in 1997 and 2006, respectively.

He was a Research Student with Saitama University and the Electrotechnical Laboratory, Tsukuba, Japan, a Visiting Associate with the Tokyo Institute of Technology, a Researcher with LABSP, BSI, RIKEN, Wakoshi, Japan. He was a JSPS Postdoctoral Research Fellow with the Tokyo Institute of Technology, from October 2007 to September 2009. Since November 1991, he has been with the Institute of Electrical Engineering "Nikola Tesla," Belgrade. His research interests include machine learning based on quantum probabilistic model, biologically inspired neural networks and their implementation in signal processing and brain modeling, and real-time control, design of software and hardware for microprocessor, and PC-based systems in power electronics and industry.

Srdjan Srdic (M'09) received the B.S.E.E., M.S.E.E., and Ph.D. degrees from the School of Electrical Engineering, University of Belgrade, Belgrade, Serbia, in 2004, 2010, and 2013, respectively.

Since 2005, he has been with the Department of Power Engineering, School of Electrical Engineering, University of Belgrade, where he is currently an Assistant Professor. His research interests include high-power converters for metals industry, power converters for renewable energy systems, and application of widebandgap semiconductor devices in power converters.

Zoran Radakovic was born in Belgrade, Serbia, on May 27, 1965. He received the B.Sc., M.Sc., and Ph.D. degrees from the Faculty of Electrical Engineering, University of Belgrade, Belgrade, in 1989, 1992, and 1997, respectively.

He was a Research and Teaching Assistant with the University of Belgrade, as Humboldt Research Fellow with the University of Stuttgart, and a Research and Development Engineer with Siemens AG, responsible for the development of cooling in Technology and Innovation Department of Transformer Division, Nuremberg, Germany. He is currently a Professor at the Faculty of Electrical Engineering, University of Belgrade. One of his research and development fields is photovoltaic technique. His research interests include power transformers, power quality, earthing systems, thermal modeling, automatic control, and photovoltaic technique.